HyspIRI Visible to Short Wavelength InfraRed (VSWIR)
Land Surface Reflectance
Algorithm Theoretical Basis Document (ATBD)

Version: April 2010

Bo-Cai Gao[1] and Robert O. Green[2]

[1]Remote Sensing Division, Code 7230, Naval Research Laboratory
4555 Overlook Avenue, SW, Washington, DC 20375

[2]Robert O. Green, NASA Jet Propulsion Laboratory
4800 Oak Grove Dr., Pasadena, CA 91109

TABLE OF CONTENTS

SUMMARY

This algorithm theoretical basis document (ATBD) describes an algorithm for retrieving the Level 2 land surface reflectance data products from the Visible ShortWave InfraRed (VSWIR) Level 1b calibrated radiance data. It is in preparation for the possible near future NASA Hyperspectral Infrared Imager (HyspIRI) mission - a Decadal Survey Mission recommended by the National Research Council (NRC). VSWIR, an imaging spectrometer covering the solar spectral region between 0.38 and 2.5 micron with a spatial resolution of 60 m, is one of the two instruments planned for the HyspIRI mission to produce global observations of multiple Earth surface attributes for a variety of terrestrial and aquatic studies.

The radiances received by the VSWIR instrument in the solar spectral region are affected by absorption and scattering effects from atmospheric gases and aerosols. In order to use the VSWIR data for quantitative studies of Earth surface properties, the atmospheric effects need to be removed. In this ATBD, we describe a radiative transfer modeling based atmospheric correction approach for the retrieval of land surface reflectances on a pixel-by-pixel basis from VSWIR data. The descriptions include all elements for corrections, such as atmospheric gases, aerosols, and thin cirrus clouds, journal literature backing up the approach, theoretical descriptions on algorithm's physics and mathematical background, and sample retrieval results from spectral imaging data collected with the NASA JPL Airborne Visible Infrared Imaging Spectrometer (AVIRIS).

1 INTRODUCTION

This document describes an algorithm for retrieving the Level 2 land surface reflectance data products from the Visible ShortWave InfraRed (VSWIR) Level 1b calibrated radiance data. It is in preparation for the possible near future NASA Hyperspectral Infrared Imager (HyspIRI) mission, a Decadal Survey Mission recommended by the National Research Council (NRC). VSWIR, an imaging spectrometer covering the solar spectral region between 0.38 and 2.5 micron with a spatial resolution of 60 m, is one of the two instruments planned for the HyspIRI mission to produce global observations of multiple Earth surface attributes for a variety of terrestrial and aquatic studies.

The radiances received by the VSWIR instrument in the solar spectral region are affected by absorption and scattering effects from atmospheric gases and aerosols. In order to use the VSWIR data for quantitative studies of Earth surface properties, the atmospheric effects need to be removed.

In this document, we describe a radiative transfer modeling based atmospheric correction approach for the retrieval of land surface reflectances on a pixel-by-pixel basis from VSWIR data. The descriptions include all elements for corrections, such as atmospheric gases, aerosols, and thin cirrus clouds, journal literature backing up the approach, theoretical descriptions on algorithm's physics and mathematical background, and sample retrieval results from the NASA JPL AVIRIS data and other imaging spectrometer data.

Background information on the concept of imaging spectrometry, atmospheric corrections over land, and the VSWIR instrument characteristics is described in Section 2. Detailed description of the land version of the hyperspectral atmospheric algorithm is presented in Section 3. Sample results from analysis of AVIRIS data are presented in Section 4. Research agenda are described in Section 5.

2 OVERVIEW AND BACKGROUND INFORMATION

The objectives of this algorithm, the historical perspective on hyperspectral atmospheric corrections over land, and the unique features of the VSWIR instrument, are described in this section.

2.1 Experimental Objective

The purpose of this algorithm is to derive surface reflectance spectra over clear land areas of the globe. The data products will be used for a variety of applications, and to answer many key science questions originally identified in the National Research Council Decadal Survey and recently refined by the HyspIRI Science Study Groups and research community. These questions include, but not limited to: What is the composition, function, and health of land and water

ecosystems? How are these ecosystems being altered by human activities and natural causes? How do these changes affect fundamental ecosystem processes upon which life on Earth depends?

2.2 Historical Perspective

2.2.1 The imaging spectrometry concept

The concept of imaging spectrometry, or hyperspectral imaging of the Earth, originated at the NASA Jet Propulsion Laboratory (JPL) in the early 1980s. Imaging spectrometers acquire images in many contiguous spectral channels such that for each picture element (pixel) a complete reflectance or emittance spectrum can be derived from the wavelength region covered (Goetz et al., 1985). Figure 1a shows an example of 3-dimensional data cube (2D spatial and 1D spectral) processed from an AVIRIS (Vane et al., 1993; Green et al., 1998) data set acquired from an ER-2 aircraft at an altitude of 20 km. Figure 1b shows a sample AVIRIS radiance spectrum. The solar radiation on the Sun-surface-sensor ray path is subject to absorption and scattering by the atmosphere and the surface. Major atmospheric water vapor absorption bands centered at approximately 0.94, 1.14, 1.38 and 1.88 µm, an oxygen absorption band at 0.76 µm, and a carbon dioxide absorption band near 2.08 µm are clearly seen in the spectrum. The shorter wavelength region below 1 µm is also affected by molecular and aerosol scattering.

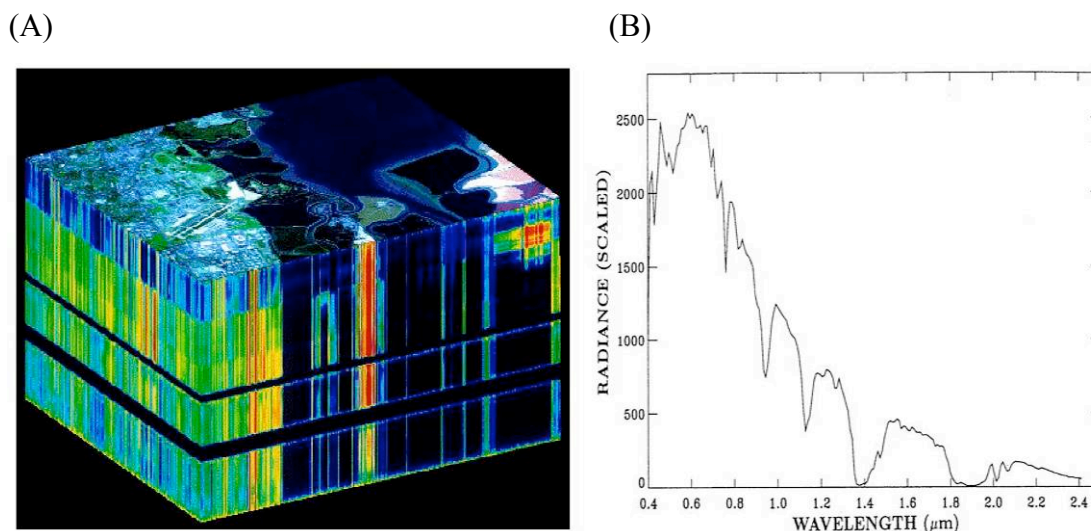(A)   (B)

Fig. 1. (a) - an example of 3-dimensional data cube (2D spatial and 1D spectral) processed from an AVIRIS data set, and (b) – a sample AVIRIS radiance spectrum over land.

There is growing interest in hyperspectral remote sensing for research and applications in a variety of fields, including geology, agriculture, forestry, coastal and inland water studies, environment hazards assessment, and urban studies (Davis et al., 2002). In order to study surface properties using imaging spectrometer data, accurate removal of atmospheric absorption and scattering effects is required. This process, called atmospheric correction, is essential to convert

radiances measured by the sensors to reflectances of surface materials. Since the mid-1980s, atmospheric correction algorithms have evolved from the earlier empirical line method and flat field method to more recent methods based on rigorous radiative transfer models. In this ATBD, all surfaces are assumed to be horizontally orientated Lambertian surfaces. In order to get the true reflectances for tilted surfaces, our retrieved reflectances need to be multiplied by factors related to the slopes and aspects of the surfaces. The term "reflectance" used here is the reflectance in a common sense. A thorough review of different reflectance quantities used in the literature, such as the bidirectional reflectance distribution function (BRDF) and directional-hemispherical reflectance, has been given by Schaepman-Strub et al. (2006).

2.2.2 Empirical atmospheric correction approaches

During the mid-1980s, several scene-based empirical approaches were developed to remove atmospheric effects from hyperspectral imaging data for the derivation of relative surface reflectance spectra. The Internal Average Reflectance (IAR) approach of Kruse (1988) calculates the average spectrum of a scene. The spectrum of any pixel in the scene is then divided by the average spectrum to estimate the relative reflectance spectrum for the pixel. This approach is mostly applicable for imaging data acquired over arid areas without vegetation. The flat field correction approach (Roberts et al., 1986) assumes that there is an area in the scene that has spectrally neutral reflectances, i.e., the spectrum has little variation with wavelength. The mean spectrum of the "flat field" is then used for the derivation of relative reflectance spectra of other pixels in the scene. Both the IAR approach and the "flat field" approach do not need any field measurements of reflectance spectra of surface targets. The derived relative reflectance spectra often have absorption features that are not present in reflectance spectra of comparable materials measured in the field or laboratory (Clark and King, 1987). The reason is that the mean spectrum of the "flat field" often contains absorption effects of surface materials and is not 100% spectrally neutral. The use of such mean spectrum in the derivation of relative reflectance spectra of other pixels can introduce broad absorption bands in the resulting spectra.

The empirical line approach (Conel et al., 1987) requires field-measurements of reflectance spectra for at least one bright target and one dark target. The imaging spectrometer data over the surface targets are linearly regressed against the field-measured reflectance spectra to derive the gain and offset curves. The gain and offset curves are then applied to the whole image for the derivation of surface reflectances for the entire scene. This method produces spectra that are most comparable to reflectance spectra measured in the field, or in the laboratory (Aspinall et al., 2002). However, if changes occur in the atmospheric properties outside the area used for the empirical line approach, which is often the case, the spectral reflectance data will contain atmospheric features.

It should be pointed out that the absolute radiometric calibration of hyperspectral imagers is not required when using these empirical approaches for the estimates of relative surface

reflectances. However, the hyperspectral imaging system must remain stable over the duration of data acquisition in order to apply these approaches.

2.2.3 Radiative transfer modeling approaches for land

Around 1987, Alexander F. H. Goetz first perceived the need for developing an atmospheric correction technique using radiative transfer modeling, given the limitations of the empirical approaches for surface reflectance retrievals. The thought was soon realized with the development of the Atmosphere Removal algorithm (ATREM) (Gao et al., 1993) for retrieving land surface reflectance spectra from hyperspectral imaging data using a theoretical modeling technique, which simulates explicitly the absorption and scattering effects of atmospheric gases and aerosols. The development of ATREM marked a major advance in imaging spectrometry. The band model version of the ATREM source code (Version 3.1) was distributed to more than 300 researchers worldwide free of any charges in the early 1990s through the Center for the Study of Earth from Space (CSES), University of Colorado at Boulder, Colorado. This made it possible for a large land remote sensing community to convert imaging spectrometer data to surface reflectances and resulted in significant acceleration of hyperspectral research activities.

Major upgrades to the ATREM code were made in the late 1990s and early 2000s. The band model was replaced with a line-by-line atmospheric transmittance model (Gao and Davis, 1997) and the HITRAN2000 line database (Rothman et al., 2003; Rothman et al., 2005). The 5S computer code (Tanre et al., 1986) was replaced with the newer version of 6S code (Vermote et al., 1994) for modeling atmospheric scattering effects. A module for modeling atmospheric NO_2 absorption effects in the $0.4 - 0.8$ μm spectral region was added. The algorithm needs to have an input for column NO_2 amount (typically about 5 x 10^{15} molecules/cm^2). The updated ATREM algorithm has been released to a small number of users for improved derivation of surface reflectances, particularly over spectral regions that have atmospheric gaseous absorption features.

There are now a number of atmospheric correction algorithms for retrieving surface reflectances from hyperspectral imaging data. These include, but are not limited to, the High-accuracy ATmospheric Correction for Hyperspectral Data (HATCH) (Qu et al., 2003), the Atmosphere CORrection Now (ACORN) (Kruse, 2004), the Fast Line-of-sight Atmospheric Analysis of Spectral Hypercubes (FLAASH) (Adler-Golden et al., 1999), the Imaging Spectrometer Data Analysis System (ISDAS) (Staenz et al., 1998), and a series of Atmospheric and Topographic Correction (ATCOR) codes (Richter, 1996; Richter, 1998; Richter and Schlaepfer, 2002). Some of the codes include more advanced features, such as spectral smoothing, topographic correction, and adjacency effect correction. These features were not included in ATREM.

2.3 Instrument Characteristics

The HyspIRI VSWIR instrument is a push broom imaging spectrometer (Mourioulis et al., 2000; Ungar, 1997) covering the solar spectral region between 0.38 and 2.5 micron in 10 nm channels. It has an accurate 60 m pixel size and 19 days of revisiting time for global mapping of land and shallow waters. The major science measurement characteristics of VSWIR are given in Table 1. The required signal to noise ratios (SNRs) at the benchmark radiances are shown in Figure 2.
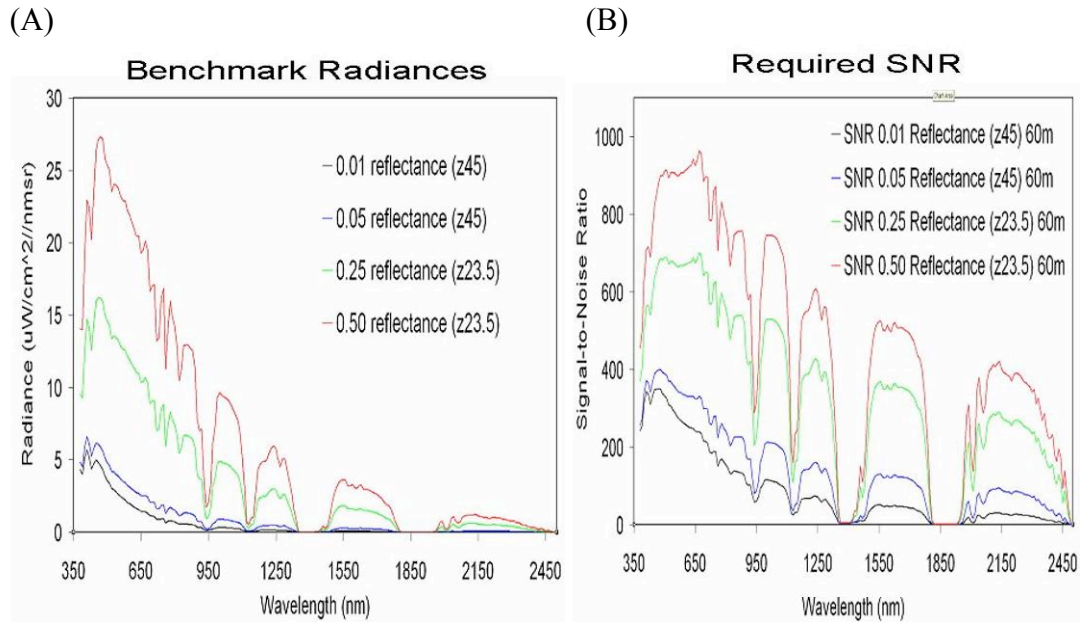
(A)   (B)

Fig. 2. Benchmark radiances (a) and the required signal to noise ratios (b).

Table 1. Major HyspIRI VSWIR science measurement characteristics.

Spectral	
Range	380 to 2500 nm in the solar reflected spectrum
Sampling	<= 10 nm {uniform over range}
Response	<= 1.2 X sampling (FWHM) {uniform over range}
Accuracy	<0.5 nm
Radiometric	
Range & Sampling	0 to 1.5 X max benchmark radiance, 14 bits measured
Accuracy	>95% absolute radiometric, 98% on-orbit reflectance, 99.5% stability
Precision (SNR)	See Fig. 2 spectral plots at benchmark radiances
Linearity	>99% characterized to 0.1 %
Polarization	<2% sensitivity, characterized to 0.5 %
Scattered Light	<1:200 characterized to 0.1%
Spatial	
Range	>150 km (12 degrees at 700 km altitude)
Cross-Track Samples	>2500
Sampling	<=60 m
Response	<=1.2 X sampling (FWHM)
Uniformity	
Spectral Cross-Track	>95% cross-track uniformity {<0.5 nm min-max over swath}
Spectral-IFOV-Variation	>95% spectral IFOV uniformity {<5% variation over spectral range}
Temporal	
Orbit Crossing	11 am sun synchronous descending
Global Land Coast Repeat	19 days at equator
Rapid Response Revisit	3 days (cross-track pointing)
Sunglint Reduction	
Cross Track Pointing	4 degrees in backscatter direction
OnOrbit Calibration	
Lunar View	1 per month {radiometric}
Solar Cover Views	1 per day {radiometric}
Dark signal measurements	1 per orbit and edge detector tracking
Surface Cal Experiments	3 per year {spectral & radiometric}
Data Collection	
Land Coverage	Land surface above sea level excluding ice sheets
Water Coverage	Coastal zone -50 m and shallower
Solar Elevation	20 degrees or greater
Open Ocean/Ice Sheets	Averaged to 1km spatial sampling
Compression	>=3.0 lossless

Because the VSWIR instrument has continuous spectral coverage at sufficiently high spectral resolution (the same as AVIRIS), the VSWIR spectral imaging data are expected to permit the positive identifications of many types of surface materials and to address most of the important science questions posed by NRC and by the HyspIRI Science Study Groups. For example, plant and phytoplankton functional types and species have biochemical and biophysical properties that are expressed as reflectance and absorption features spanning the spectral region from 0.38 to 2.5 micron. Individual narrow bands do not capture the diversity of biochemical and biophysical signatures of plant functional types or species. Changes in the chemical and physical configuration of ecosystems are often expressed as changes in the contiguous spectral signatures that relate directly to plant functional types, vegetation health, and species distribution. The contiguous spectral measurements from VSWIR would allow researchers to address many outstanding questions related to vegetation. Other constituents of the Earth system, such as rocks and minerals, soils, snow, also have various spectral characteristics. The VSWIR spectroscopic measurement will allow researchers to address the corresponding science questions.

The VSWIR spectral measurement has another important advantage, namely the data contain sufficient amount of information about atmospheric water vapor, aerosols, and thin cirrus clouds. It is possible to remove atmospheric effects from the VSWIR data themselves (Gao et al., 1993; Gao et al., 1998).

3 ALGORITHM DESCRIPTION

The proposed algorithm for retrieving the Level 2 land surface reflectance data products from VSWIR Level 1b calibrated radiance data is described from both theoretical and practical point of view in this section.

3.1 Theoretical Description

3.1.1 Physics of the problem

The solar radiation on the sun-surface-sensor path is affected by absorption and scattering effects from atmospheric gases and aerosols. Accurate modeling of these effects is required in order to derive surface reflectance spectra from imaging spectrometer data. Among the approximately thirty atmospheric gases, only eight gases, namely water vapor (H_2O), carbon dioxide (CO_2), ozone (O_3), nitrous oxide (N_2O), carbon monoxide (CO), methane (CH_4), oxygen (O_2), and nitrogen dioxide (NO_2) produce observable absorption features in imaging spectrometer data over the range 0.4 to 2.5 mm with a spectral resolution between 1 and 20 nm. Figure 3 shows examples of simulated atmospheric transmittances for the eight gases. Approximately half of the spectral region between 0.4 and 2.5 mm is affected by atmospheric water vapor absorption. The absorption effects from the other seven gases are generally located in much narrower wavelength intervals.
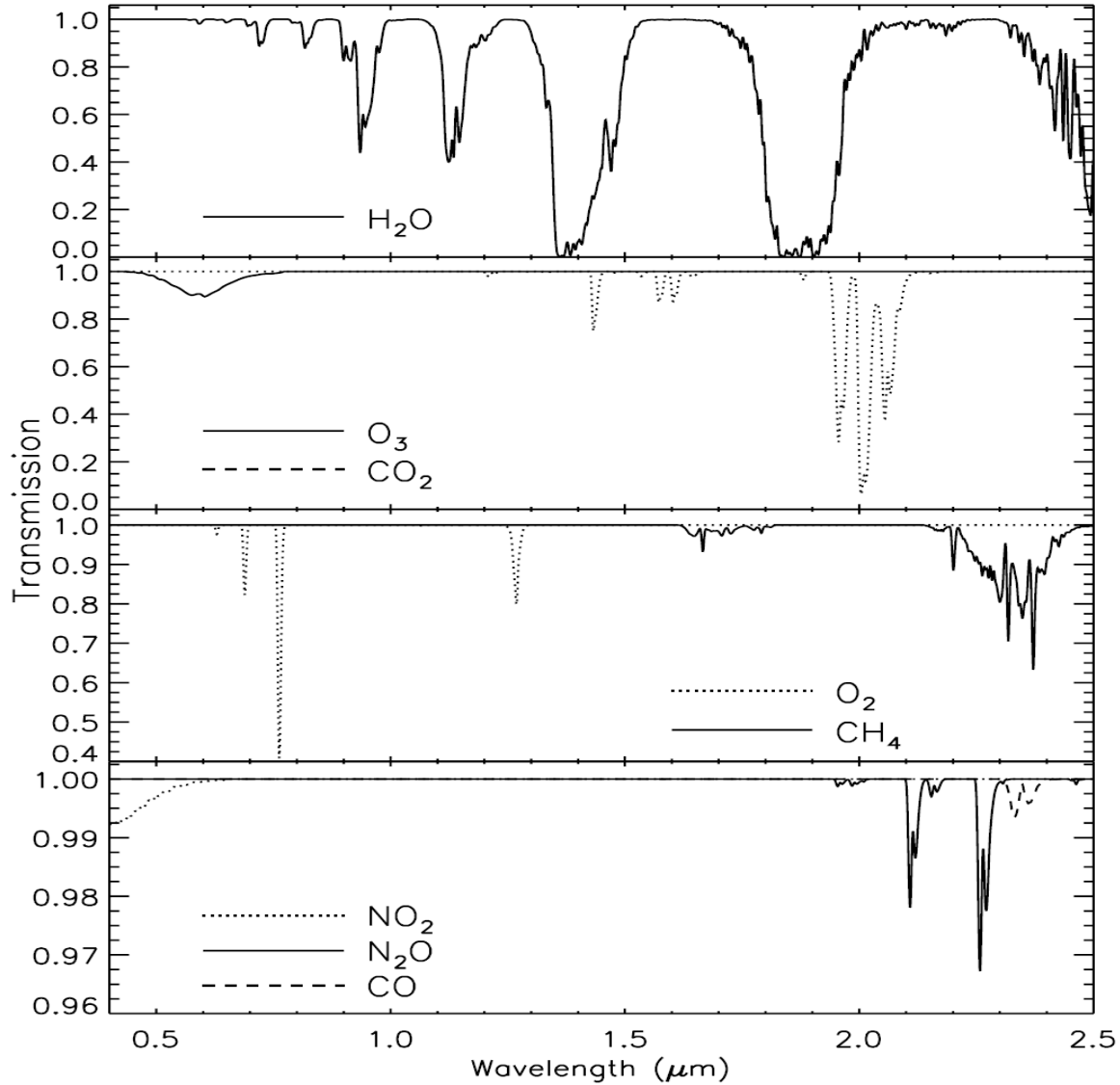
Fig. 3. Simulated transmittance spectra of atmospheric water vapor, carbon dioxide, ozone, nitrous oxide, carbon monoxide, methane, oxygen, and nitrogen dioxide.

Atmospheric gaseous molecules and aerosols scatter solar radiation. The short wavelength region between 0.4 and 0.7 mm is strongly affected by molecular scattering (Rayleigh scattering). Its effect decreases rapidly with increasing wavelength (l^{-4}). The aerosol scattering effect also decreases with increasing wavelength, but at a slower rate (typically l^{-2} to l^{-1}).

3.1.2 Mathematical description of the algorithm

The radiances measured with an imaging spectrometer from a satellite include atmospheric path radiances (due to Rayleigh and aerosol scattering) and surface-reflected solar radiances.

These radiances are often converted to "apparent reflectances" (e.g., Tanre et al., 1986; Gao et al., 1993). The definition of apparent reflectance is given by

$$r^*_{obs}(l,q,f,q_o,f_o) = p\,L_{obs}(l,q,f,q_o,f_o) \,/\, [m_o\,F_o(l)], \tag{1}$$

where q_o is the solar zenith angle, f_o the solar azimuth angle, q the sensor zenith angle, f the sensor azimuth angle, l wavelength, L_{obs} the radiance measured at the satellite, F_o the solar flux at the top of the atmosphere when the solar zenith angle is equal to zero, and m_o the cosine of solar zenith angle. Apparent reflectance is a measure of the reflectivity for the atmosphere and surface system. According to Tanre et al. (1986), when the surface is assumed to be Lambertian and the adjacency effect is neglected, $r^*_{obs}(l,q,f,q_o,f_o)$ can be expressed approximately as:

$$r^*_{obs}(l,q,f,q_o,f_o) = [r^*_{atm}(l,q,q_o,f_o) + t_d(l,q_o)\,t_u(l,q)\,r(l)/(1 - s(l)r(l)\,)]\,T_g(l,q,q_o), \tag{2}$$

where r^*_{atm} is the path reflectance, t_d the downward scattering transmittance, t_u the upward scattering transmittance, s the spherical albedo of the atmosphere, r the surface reflectance, and T_g the total gaseous transmittance in the Sun-surface-sensor path. The first term in the bracket, r^*_{atm}, is the contribution from atmospheric scattering to the measured apparent reflectance. The second term in the bracket, $t_d\,t_u\,r/(1 - s\,r)$, is the contribution from surface reflection to the measured apparent reflectance. The term T_g contains absorption bands of all atmospheric gases, as shown in Fig. 3. Eq. (2) treats the atmospheric scattering and gaseous absorption processes as two independent processes. The coupling effects between the two are neglected. In the real atmosphere, the scattering and absorption processes occur simultaneously. The coupling effects are small in regions where the atmospheric gaseous absorptions are weak and in regions where the scattering effects are small.

Solving Eq. (2) for surface reflectance r and simplifying the notations for relevant quantities yields

$$r = (r^*_{obs}/T_g - r^*_{atm}) \,/\, [t_d\,t_u + s\,(r^*_{obs}/T_g - r^*_{atm})\,]. \tag{3}$$

By simulating the atmospheric quantities T_g, r^*_{atm}, t_d, t_u, and s with radiative transfer models, the reflectance (assumed for the horizontal Lambertian surface), r, can be retrieved from the measured radiance, L_{obs}, using Eqs. (1) and (3). There are now limited case studies (e.g., Kaufman et al., 1997; Guanter et al., 2005) on the retrieval of aerosol models and optical depths from imaging data.

Thin cirrus clouds frequently contaminate satellite measured images. Through analysis of the NASA JPL AVIRIS data, we have found that narrow channels located within the 1.38- and 1.88-micron atmospheric band centers are very effective in detecting thin cirrus clouds (Gao and Kaufman, 1995). The mechanisms for the cirrus detection are straight forward. In the absence of cirrus clouds, AVIRIS channels near 1.38 μm receive little scattered solar radiance by the

surface and the low level water clouds because of the total absorption of solar radiation by atmospheric water vapor located above them. When cirrus clouds are present, however, these channels receive scattered solar radiance by the cirrus clouds, which contrast well on the nearly black background.

Because the 1.38-micron channels are slightly affected by absorption from water vapor located above and within thin cirrus clouds, the water vapor effects must be removed in order to use the 1.38-micron channels for quantitative correction of thin cirrus effects in other channels (Gao et al., 1998; Gao et al., 2002). For thin cirrus clouds, we assume that a homogeneous thin cirrus layer is located above a "virtual surface", which includes the effects of Rayleigh scattering and land or ocean surface reflection and scattering. Omitting for convenience the wavelength (l) and cosine-solar-zenith-angle (m_0) dependencies, we denote the "apparent reflectance" at the satellite as $r^*_{obs} = (p\, L_{obs} / m_0\, F_0)$ (see also Eq. (1)). Accounting for transmission through the cirrus cloud and multiple reflections between cloud and the "virtual surface", we have the following relationship (similar to what is done for aerosol correction, e.g., Fraser and Kaufman, 1985):

$$r^*_{obs} = r_c + T_c\, r_v / (1 - S_c\, r_v) \tag{4}$$

where r_c is the reflectance of the cirrus cloud, T_c is the two-way transmission (direct + diffuse) through the cloud, r_v is the reflectance of the "virtual surface", and S_c is the cloud-base reflectance of upward radiation. Because $S_c\, r_v << 1$ for thin cirrus, Eq. (4) can be simplified to:

$$r^*_{obs} = r_c + T_c\, r_v \tag{5}$$

In order to remove the cirrus effect from the satellite measurement r^*_{obs}, namely to derive r_v based on Eq. (5), cirrus reflectance r_c and transmittance T_c must be known.

Through analysis of AVIRIS data, we have found that cirrus reflectance r_c for AVIRIS channels between 0.4 and 1.0 µm is linearly related to r_c at 1.375 µm, i.e.,

$$r_c = r_c(1.375\ \mu m) / K_a, \quad 0.4 < l < 1.0\ \mu m \tag{6}$$

where K_a is an empirical parameter derived from AVIRIS data themselves. It is essentially the 1.375-µm channel transmittance for water vapor above and within cirrus clouds. The weak ice absorption at 1.375 µm also decreases slightly the K_a value. Substituting (6) into (5), we obtain:

$$T_c\, r_v = r^*_{obs} - r_c(1.375\ \mu m) / K_a, \quad 0.4 < l < 1.0\ \mu m \tag{7}$$

The image of $T_c r_v$ is referred to as the "cirrus-path-radiance-corrected" image in this ATBD. It is similar to the "virtual surface" reflectance image of r_v due to large transmittances of thin cirrus clouds (T_c is usually greater than 0.9). Because VSWIR and AVIRIS have similar spectroscopic properties, the formulation for corrections of thin cirrus effects from AVIRIS data applies equally well to the VSWIR data.

3.1.3 Algorithm implementations

The procedures adopted in the updated version of ATREM code (Gao and Davis, 1997) for correction of atmospheric gas absorption and molecular and aerosol scattering effects will be followed in the present algorithm implementation for the retrieval of land surface reflectances from VSWIR data. This version of ATREM code allows the retrieval of surface reflectance spectra from imaging spectrometer data, such as those collected with AVIRIS, without the need for field-measurements of reflectance spectra. Because water vapor is quite variable spatially, the integrated water vapor amount is derived on a pixel by pixel basis from the 0.94- and 1.14-µm water vapor absorption bands using a channel ratio technique (Gao et al., 1993). The water vapor transmittance spectrum in the complete solar spectral region between 0.4 and 2.5 mm is then simulated using a line-by-line code and the derived water vapor values. Similarly, the transmission spectra of carbon dioxide (CO_2), ozone (O_3), nitrous oxide (N_2O), carbon monoxide (CO), methane (CH_4), and oxygen (O_2) in the 0.4-2.5 µm region are simulated based on the solar and observational geometry. The scattering effect due to atmospheric molecules and aerosols is modeled with the 6S computer code (Vermote et al., 1994). In order to model the aerosol effect, users need to select an aerosol model and a surface visibility. The measured radiances are divided by solar irradiances above the atmosphere to obtain the apparent reflectances. The surface reflectances are derived, according to Eq. (3), from the apparent reflectances using the simulated atmospheric gaseous transmittances and the simulated molecular and aerosol scattering data.

In order to use the 1.38-micron channels for quantitative correction of thin cirrus effects in other channels, the absorption effects by water vapor above and within cirrus clouds must be taken into consideration. The water vapor transmittance factor, K_a, in Eq. (6) can be obtained from a scatter plot between the 1.38-mm channel and a channel in atmospheric window region as illustrated in Figure 4. The slope in the left portion of the scatter plot is a good estimate of K_a (Gao et al., 1998). An empirical algorithm for the derivation of cirrus reflectances, and for subsequent correction of thin cirrus scattering effects, has already been implemented for processing MODIS data (Gao et al., 2002). We will implement a similar algorithm for estimating thin cirrus reflectances in the $0.4 - 1.0$ mm region using the empirically derived K_a value and Eq. (6). We will then correct for thin cirrus scattering effects from VSWIR channels below 1 micron.
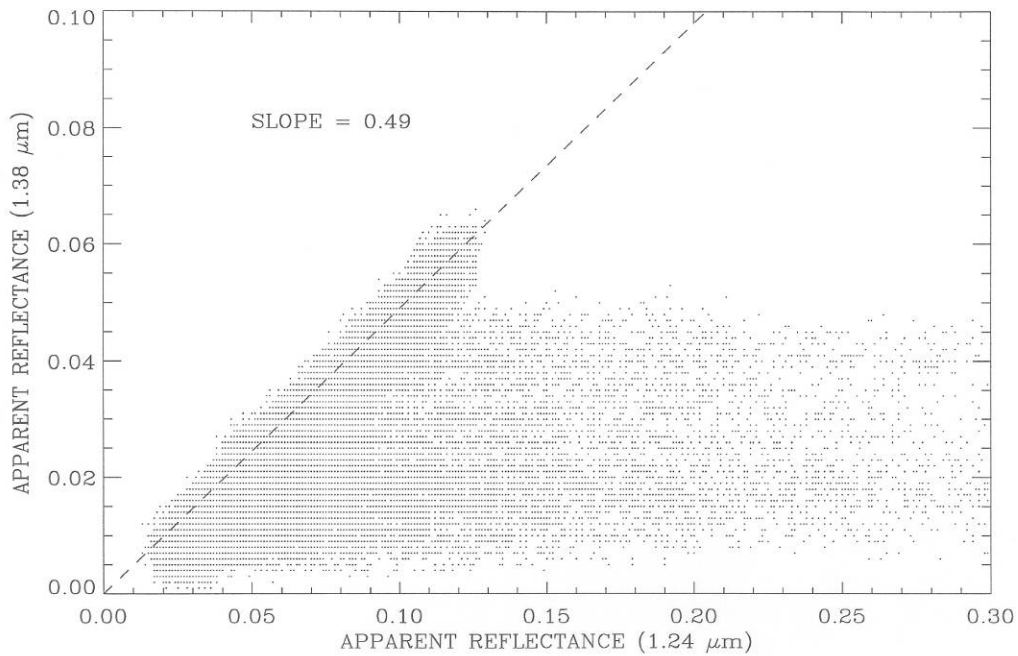
Fig. 4. A scatter plot between apparent reflectances at 1.38 mm and 1.24 mm from an AVIRIS data set acquired over the Gulf of Mexico. The slope in this plot is a good estimate of the upper lever water vapor transmittance factor.

3.1.4 Descriptions of input and output data

The VSWIR Level 2 land surface reflectance algorithm requires input data sets from the standard VSWIR L1b calibrated radiance data cubes and associated ancillary data. The radiance data cubes can be stored in three formats: BSQ (band sequential), BIL (band interleave by line), and BIP (band interleave by pixel). The most preferred format is BIL, the natural format of push broom imaging spectrometers. The inputs from ancillary data are solar zenith angle, solar azimuth angle, view zenith angle, view azimuth, and surface elevation. Optional input data include column atmospheric ozone and nitrogen dioxide amounts, atmospheric aerosol models and optical depths (or surface visibility). Default values based on climatology will be used if the optional input data are not available.

The output VSWIR Level 2 data sets include surface reflectance data cubes in any one of the three formats (BSQ, BIL, and BIP), column water vapor images, and quality assurance (QA) parameter images. The QA parameters can contain a variety of information about each pixel and the corresponding data processing stream. We intend to use short integers (I*2, 16 bits) to store the QA parameters.

3.1.5 Variance and uncertainty estimates

Several sources of errors in surface reflectance retrievals from imaging spectrometer data have been described by Gao et al. (1992). The sources of errors include:

1. Uncertainty in the linearity of surface reflectances between 0.8 and 1.24 micron.
2. Uncertainty in the sensor calibration.
3. Uncertainty in the atmospheric radiative transfer codes.
4. Uncertainty in the vertical atmospheric temperature and moisture profiles.
5. Uncertainty in the assumed aerosol models and optical depths (or visibility).

A major error source is the uncertainty in the assumed aerosol models and optical depths. Although techniques for aerosol retrievals over land have been improved in recent years, we believe that the retrieved aerosol parameters are not sufficiently accurate for use in operational corrections of aerosol effects from imaging spectrometer data on a pixel-by-pixel basis. In many situations, the aerosol products over land retrieved from passive optical remote sensing data are not quite right. For the visible spectral region, an error of 0.1 in assumed aerosol optical depths introduces an error of approximately 0.01 in the retrieved surface reflectances (Hansen and Travis, 1974). The reflectance error is smaller for longer wavelength channels because aerosol effects generally decrease with increasing wavelengths. Besides, the aerosol absorption and scattering can somewhat mutually compensate (Fraser and Kaufman, 1985). Based on these analyses and on the fact that the land surfaces are generally bright, we anticipate that the errors in derived land surface reflectances under typical atmospheric conditions by assuming climatologic aerosol models and optical depths will be relatively small. However, under heavy smoke conditions and for major dust events, the retrieved land surface reflectance errors can be quite significant if the climatological aerosol information is assumed.

3.2 Practical Considerations

Considerations of numerical computation, programming, and exception handling are presented in this section.

3.2.1 Numerical computation considerations

Problems with numerical stability and round-off errors are not expected with this algorithm.

3.2.2 Programming/procedural considerations

In the present implementation of ATREM code, a total of 60 gaseous transmittance spectra for different water vapor amounts are calculated for each scene and stored on memory for

internal use during the retrieval of surface reflectance spectra for the scene. The simulation of the 60 spectra that match the wavelengths and spectral resolution of a given imaging spectrometer takes quite a bit of CPU time. We plan to modify the ATREM code so that the 60 spectra are calculated only once for each spectrometer, and save the spectra onto hard disks for later use.

4 SAMPLE RESULTS

Land surface reflectances have been derived from AVIRIS and other imaging spectrometer data over the past two decades with several atmospheric correction algorithms. Sample results and applications are presented in this section.

Figure 5a shows an AVIRIS radiance spectrum acquired over a vegetated area in the Konza Prairie in Kansas on August 31, 1990. Figure 5b shows the retrieved reflectance spectrum with an early version of the ATREM code. Because of the total absorption in the strong 1.38- and 1.88-µm water vapor bands, it is not possible to recover the surface reflectances near the centers of the two bands. Therefore, no reflectances are shown in Fig. 5b in these regions. The green reflectance peak near 0.55 µm, the chlorophyll absorption feature centered near 0.67 µm, and the weak liquid water bands centered near 0.98 and 1.2 µm are all evident. The features in this spectrum are very similar to reflectance spectra of vegetation measured in the laboratories.
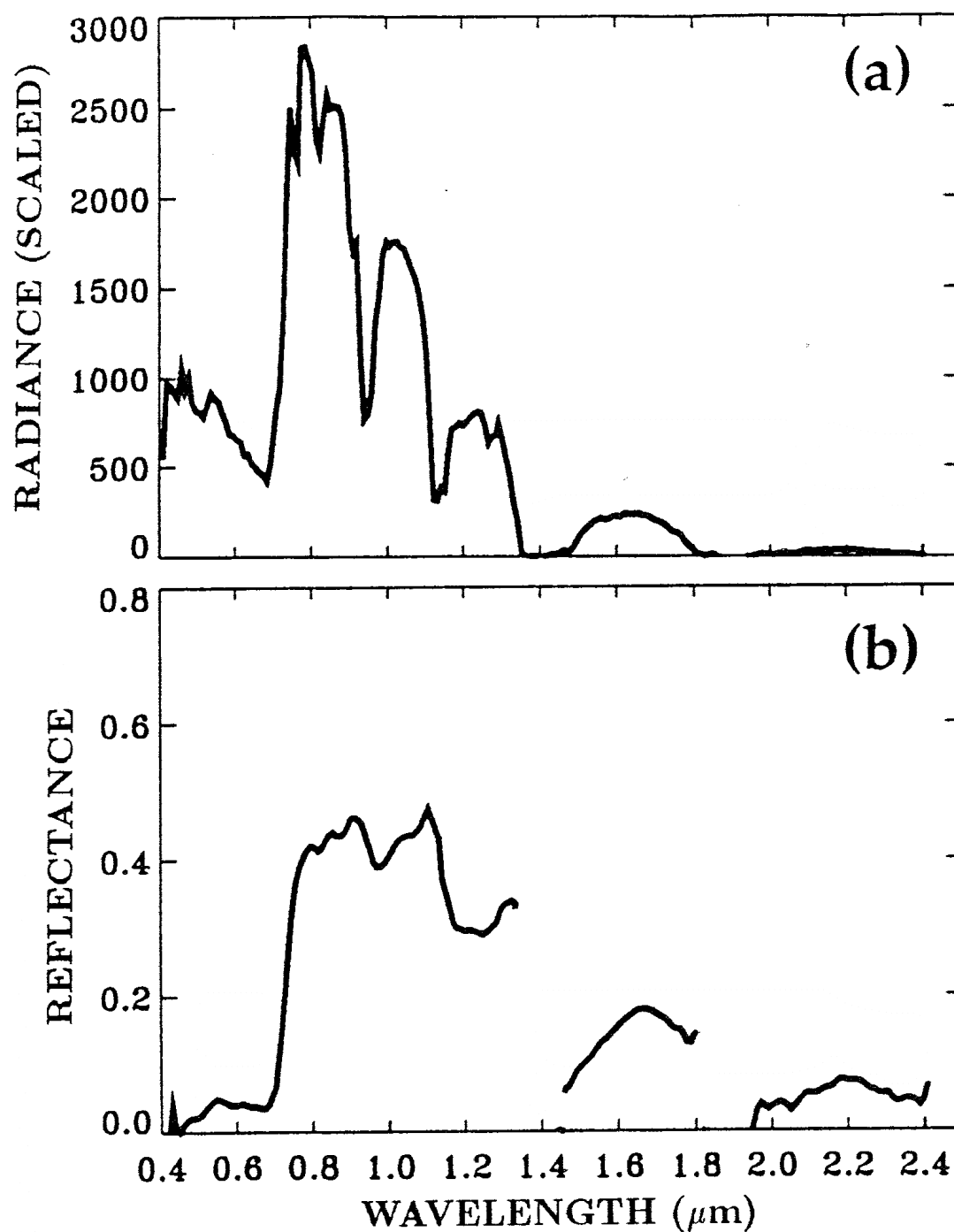
Fig. 5. (a): An AVIRIS spectrum acquired over a vegetated area in the Konza Prairie in Kansas on August 31, 1990, and (b) the corresponding retrieved reflectance spectrum. The weak liquid water absorption bands near 0.98 and 1.20 μm are seen in (b).

Figure 6a shows an AVIRIS spectrum over an area covered by the mineral kaolinite. The data were measured on July 23, 1990 over Cuprite, Nevada. Figure 6b shows surface reflectances

derived from the model. Most of the atmospheric absorption features seen in Fig. 6a are removed in Fig. 6b. The characteristic kaolinite doublet feature, resulting from the Al-OH transitions, near 2.17 µm is clearly seen in Fig. 6b.
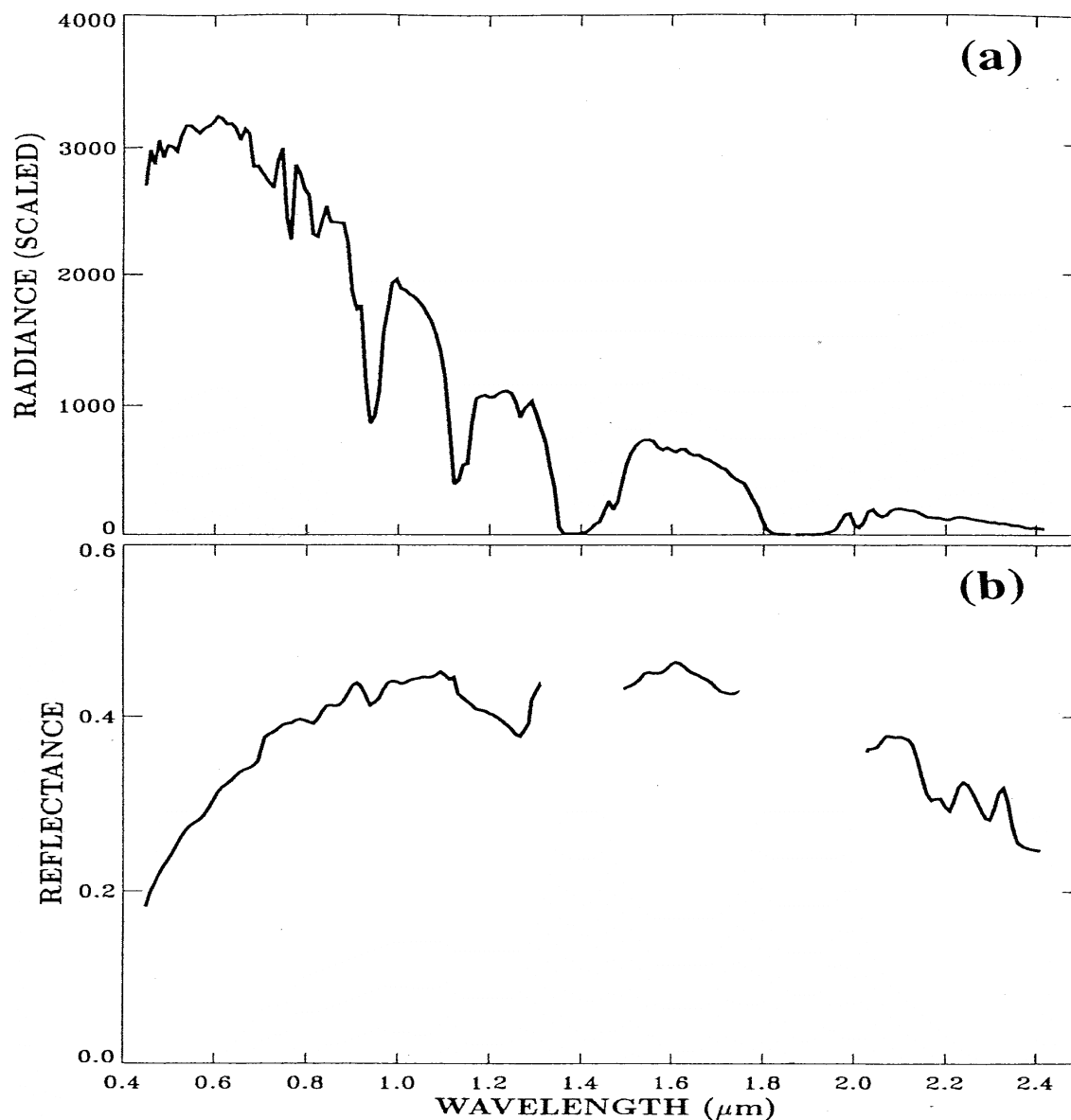

Fig. 6. (a): An AVIRIS spectrum acquired over an area covered by the mineral kaolinite in Cuprite, Nevada on July 23, 1990, and (b): the corresponding retrieved reflectance spectrum. The characteristic kaolinite doublet feature near 2.17 µm is clearly seen in (b).

High spatial resolution column atmospheric water vapor amounts and vegetation liquid water vapor can be derived from AVIRIS data in the 0.86 – 1.25 micron spectral region (Gao and Goetz, 1990). Figure 7 shows examples of column water vapor retrievals made by R. Green of NASA JPL from a time series of AVIRIS data acquired over Rogers Dry Lake, California. The visible channel images in the upper row demonstrate that the AVIRIS data were collected under very clear atmospheric conditions. The water vapor images in the lower row show detailed spatial distributions of water vapor over Rogers Dry Lake, a Space Shuttle landing site.
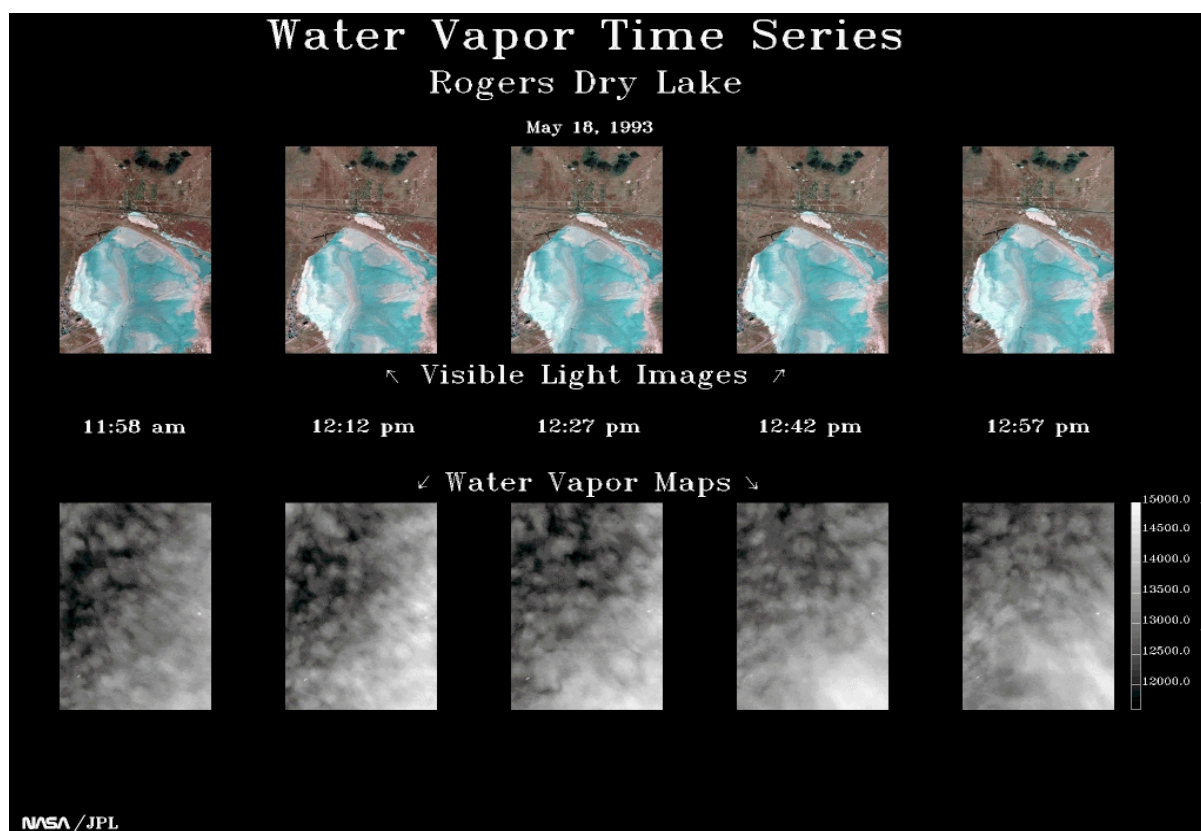

Fig. 7. Top row: 5 sets of AVIRIS visible channels images acquired over Rogers Dry Lake, California on May 18, 1993; and bottom row: the corresponding water vapor maps. The detailed spatial distributions of water vapor over the areas are seen clearly in the bottom row images.

Figure 8 shows examples of cirrus detection and corrections with a narrow channel located within the strong water vapor absorption region near 1.38 mm. Fig. 8a is an AVIRIS RGB image acquired over Bowie, Maryland in the summer of 1997. Surface features appear blurred because of the presence of thin cirrus clouds. Fig. 8b is the 1.38-mm channel image of the same scene. Only the upper level thin cirrus clouds are seen. The surface features seen in Fig. 8a disappear completely in Fig. 8b because of absorption of water vapor beneath cirrus. Fig. 8c is the cirrus corrected RGB image. The corrections were made using the procedures outlined in Section 3 of

this ATBD. By comparing Fig. 8c with Fig. 8a, it is seen that the surface features are seen much better after the removal of thin cirrus effects.
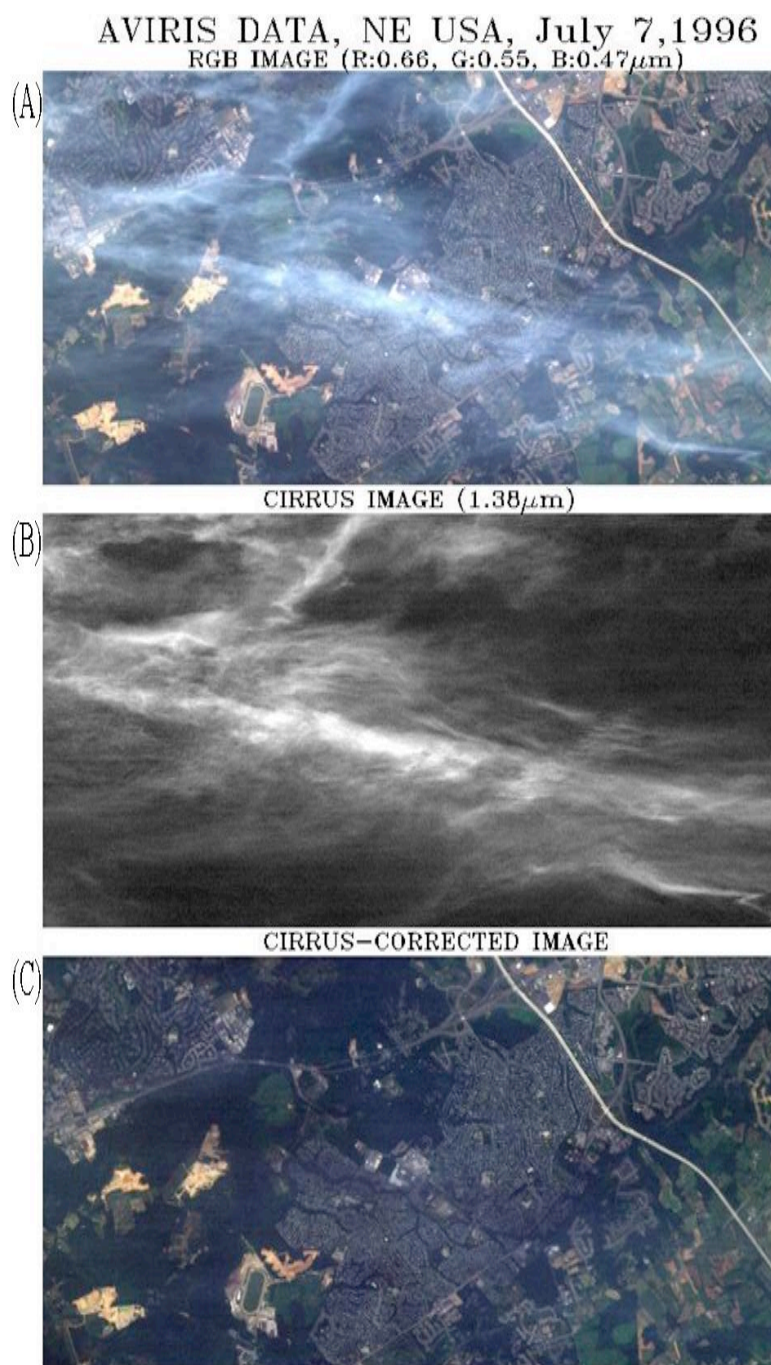

Fig. 8. An AVIRIS RGB image acquired over Bowie, Maryland in the summer of 1997 (a), the 1.38-micron image (b), and the cirrus-corrected RGB image (c).

The land surface reflectance spectral data retrieved from AVIRIS data with several atmospheric correction algorithms have been used in many applications, including those in geology, hydrology, and vegetation studies. Figure 9 shows examples of mineral mapping by R. Clark and G. Swayze at USGS in Denver, Colorado from ATREM derived surface reflectance spectra plus additional re-normalization based on field spectral measurements over a single ground calibration site (Clark et al., 1995). Over 100 types of minerals have been successfully mapped over Cuprite, Nevada from the AVIRIS data set.
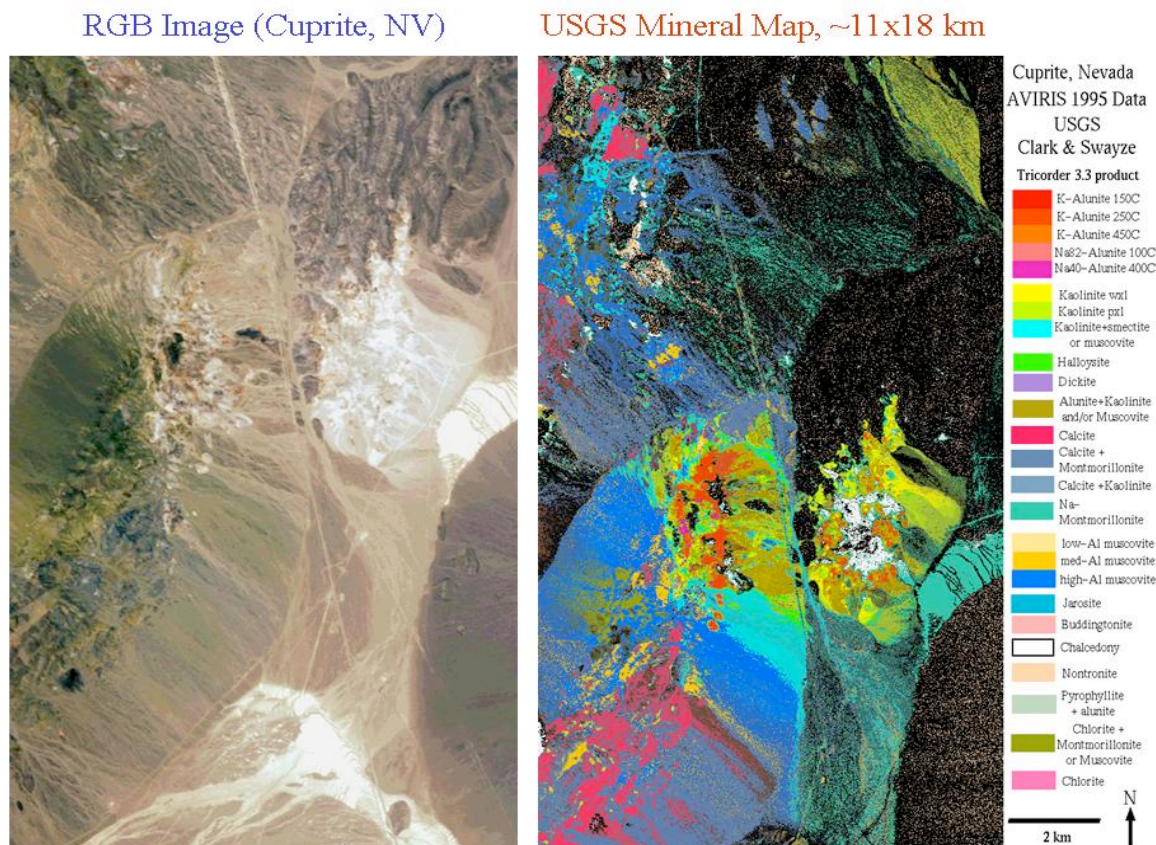

Fig. 9. An AVIRIS RGB image of Cuprite, Nevada (left plot), and a mineral map (right plot) of the site produced by USGS researchers in Denver, Colorado.

Figure 10 and 11 show examples of studying snow properties (Dozier et al., 2009) from imaging spectrometry. In Fig. 10, the fractional snow covered areas in the Tokopah Basin, Sierra Nevada, for three dates in the 1997 snowmelt season: (a) 05 May 1997, (b) 21 May, (c) 18 June, are shown. Fig. 11 shows the changes in grain size for the same period; the grain sizes are smaller in the middle image because of several small storms between 05 May and 21 May. These maps of fractional snow cover and grain size/albedo were used to drive a distributed snowmelt model.
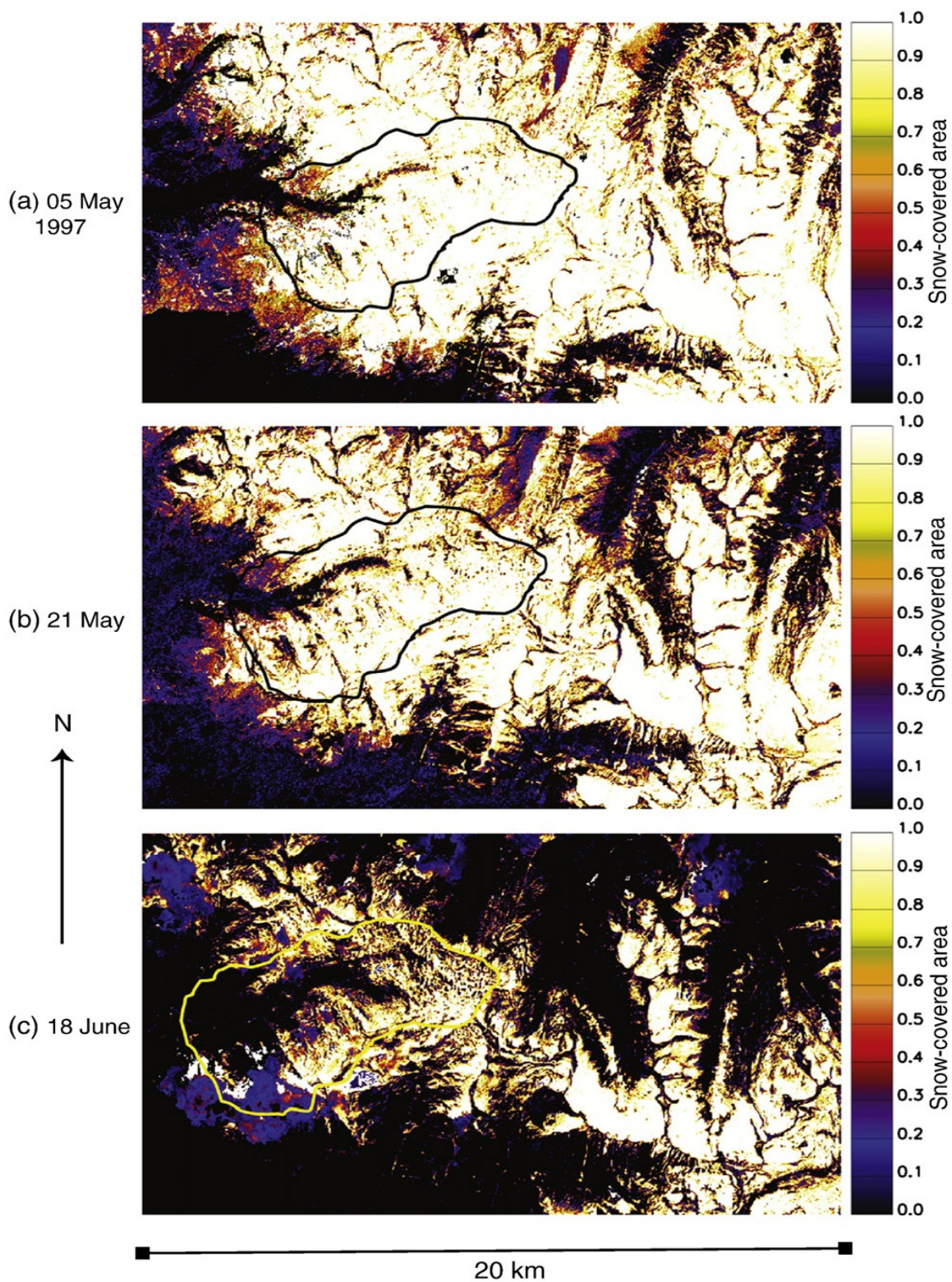
Fig. 10. Snow-covered area in the Tokopah Basin, Sierra Nevada, for three dates in the 1997 snowmelt season: (a) 05 May 1997, (b) 21 May, (c) 18 June.
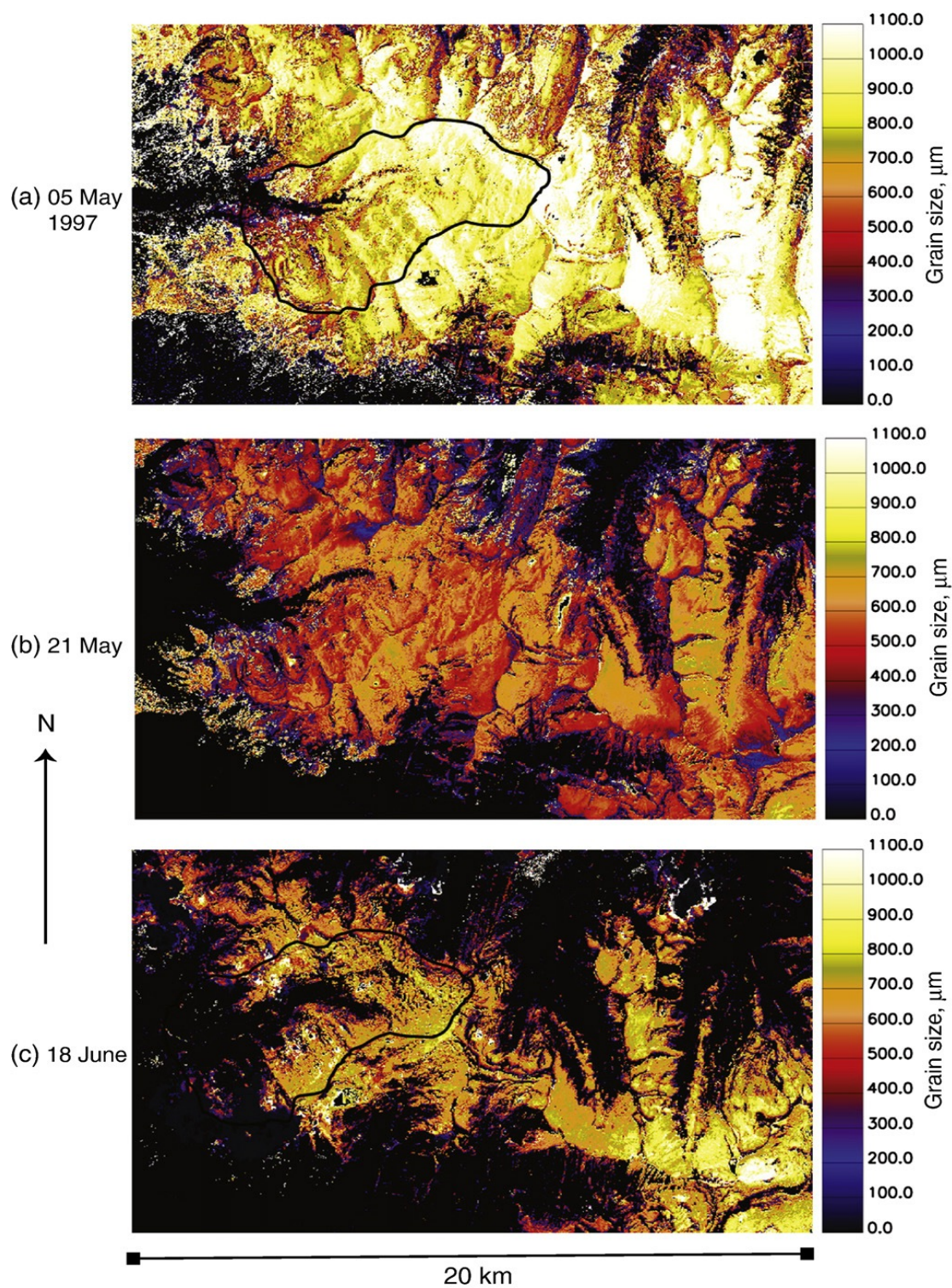
Fig. 11. Snow grain size for the snow-covered area images in Fig. 10: (a) 05 May 1997, (b) 21 May, (c) 18 June. Grain size became finer after the 05 May image because of several small storms.

Figure 12 and 13 show examples of characterizing canopy biochemistry from imaging spectroscopy (Kokaly et al., 2009). Fig. 12 is a map of forest cover types in Yellowstone National Park from AVIRIS data (Kokaly et al., 2003). Fig. 13 (Asner and Vitousek, 2003) shows leaf nitrogen concentrations and canopy water in a 1360-hectare area of Hawaii Volcanoes National Park, using AVIRIS and photon transport modeling.
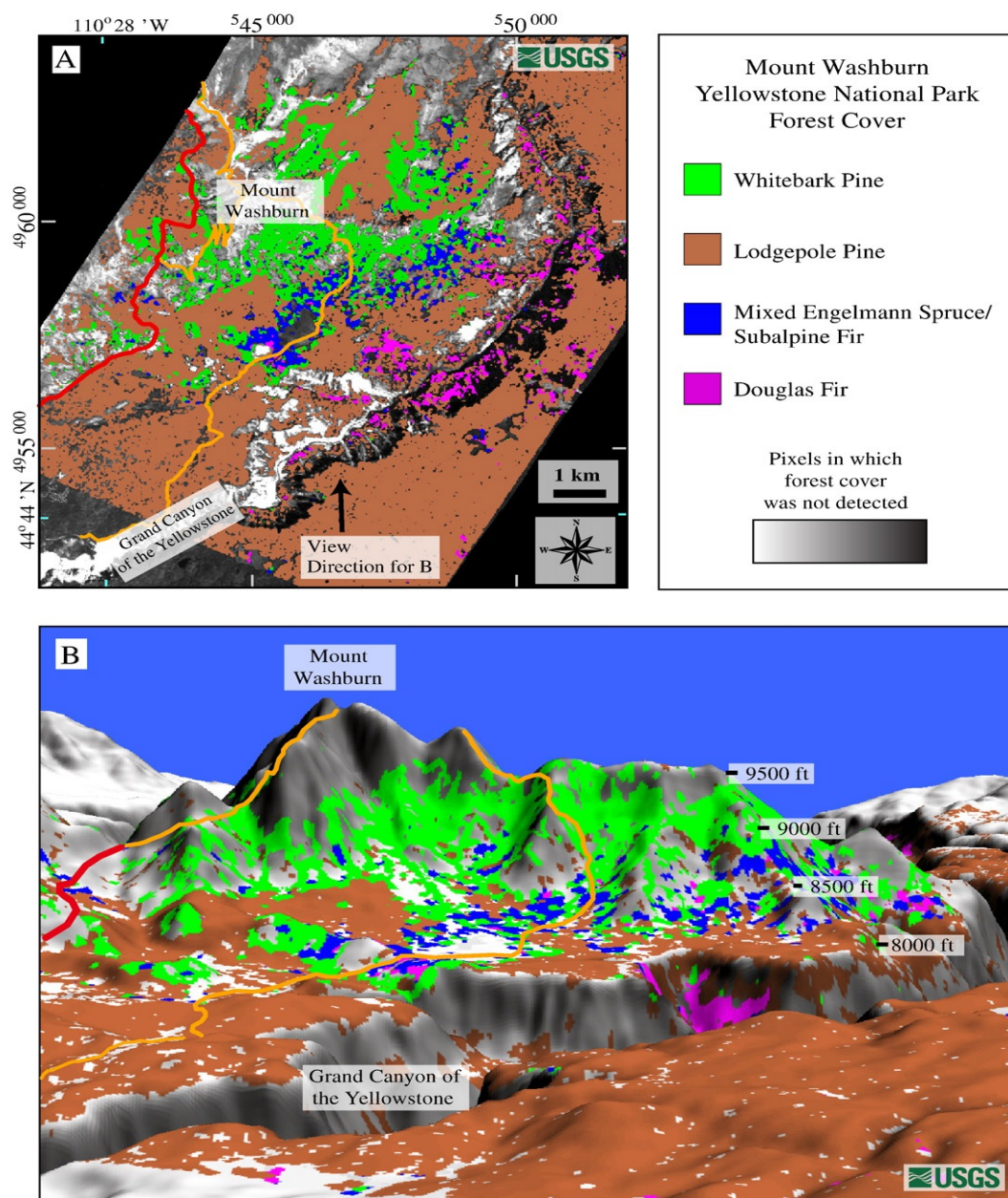

Fig. 12. Map of forest cover types in the MountWashburn area of Yellowstone National Park, derived from AVIRIS data collected in 1996. Park roads and trails are indicated in red and orange lines, respectively. A) Map projection is UTM zone 12 north with NAD83 datum. B) Perspective view towards north as indicated on A.
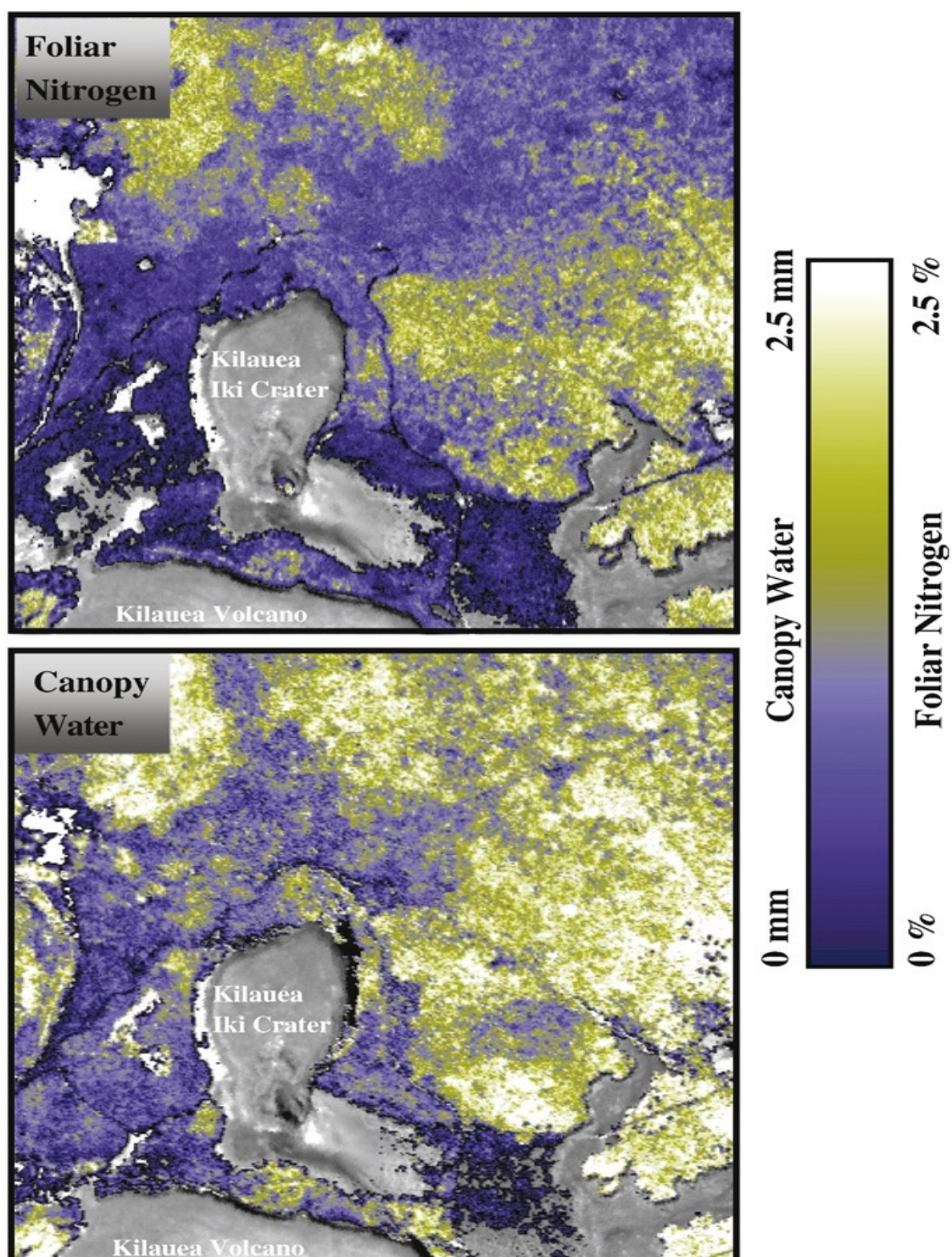
Fig. 13. Leaf N concentrations and canopy water in a 1360-hectare area of Hawaii Volcanoes National Park, using AVIRIS and photon transport modeling.

5 RESEARCH AGENDA

Because most land surfaces have complex spectrally and spatially dependent reflectivities in the visible and near infrared region, it is often difficult to decouple the atmospheric signal from the surface signal (King et al., 1998). The surface reflectances for both land and ocean in the near UV region around 0.38 micron are generally low and uniform, this spectral region can be very useful for remote sensing of aerosols, particularly under heavy smoke and dusty conditions (Torres et al., 1998;; Holler et al., 2004). The left panel in Figure 10 shows a true color RGB radiance image acquired with the Japanese GLI instrument over eastern China and Korean peninsula. The right panel shows the ratio image (0.4mm/0.38mm) for the same scene. Dust features in the ratio image are seen very nicely. There is no discontinuity in the land/water boundary area. The ratio image demonstrates clearly the sensitivity of the near-UV channels to the aerosol loading. The VSWIR instrument has continuous spectral coverage from 0.38 mm to 2.5 mm. Through further research with data acquired in the near-UV and visible regions, new techniques on aerosol retrievals over land, particularly for the heavy smoke and dusty conditions can be developed in the future.
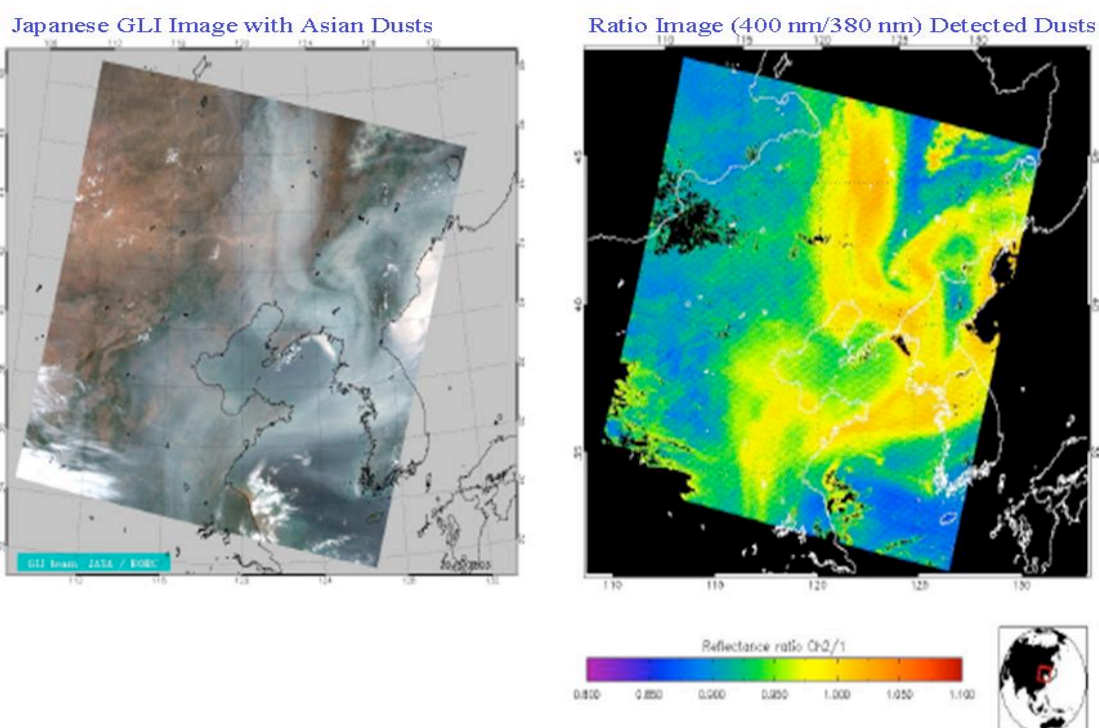

Fig. 10. Left panel: GLI level 1B geolocated RGB composite imagery from three visible channels (678nm, 545nm, 460nm) for May 20, 2003 around eastern China and the Korean peninsula; Right panel: GLI reflectance ratio (400nm/380nm) image for the same scene. The ratio image demonstrates the sensitivity of the near-UV channels to the aerosol loading.

6 REFERENCES

Adler-Golden, S. M., et al. (1999). Atmospheric correction for short-wave spectral imagery based on MODTRAN4, in Summaries of the Eighth JPL Airborne Earth Science Workshop (Editor: R. O. Green), *JPL Publication 99-17, 1*, 21-29, Jet Propul. Lab., Pasadena, California.

Asner, G. P., & Vitousek, P. M. (2005). Remote analysis of biological invasion and biogeochemical change. *Proceedings of the National Academy of Sciences of the United States of America, 102*, 4383−4386.

Aspinall, R. J., Marcus, W. A., & Boardman, J. W. (2002). Considerations in collecting, processing, and analyzing high spatial resolution hyperspectral data for environmental investigations, *Journal of Geographical Systems, 4*, 15-29.

Clark, R. N., Swayze, G. A., Heidebrecht, K. B., Green, R. O., & Goetz, A. F. H. (1995). Calibration of surface reflectance of terrestrial imaging spectrometry data: Comparison of methods, in Summaries of the 5th Annual JPL Airborne Earth Science Workshop (R. O. Green, ed.), *JPL Publication 95-1, 1*, 41-42, Jet Propulsion Laboratory, Pasadena, CA.

Clark, R. N., & King, T. V. V. (1987). Causes of spurious features in spectral reflectance data, in Proceedings of the 3rd Airborne Imaging Spectrometer Data Analysis Workshop (G. Vane, Ed.), *JPL Publ. 87-30,* 49-61, Jet Propulsion Laboratory, Pasadena, CA.

Conel, J. E., Green, R. O., Vane, G., Bruegge, C. J., & Alley, R. E. (1987). AIS-2 radiometry and a comparison of methods for the recovery of ground reflectance, in Proceedings of the 3rd Airborne Imaging Spectrometer Data Analysis Workshop (G. Vane, Ed.), *JPL Publ. 87-30*, 18-47, Jet Propulsion Laboratory, Pasadena, CA.

Davis, C. O., Bowles, J., Leathers, R. A., Korwan, D., Downes, T. V., Snyder, W. A., Rhea, W. J., Chen, W., Fisher, J., Bissett, W. P., & Reisse, R. A. (2002). Ocean PHILLS hyperspectral imager: design, characterization, and calibration, *Optics Express, 10*, 210-221.

Dozier, J., Green, R. O., Nolin, A. W., and Painter, T. H. (2009). Interpretation of snow properties from imaging spectrometry. *Remote Sensing of Environment, 113*, S25−S37.

Fraser, R.S. and Kaufman, Y. J. (1985). The relative importance of aerosol scattering and absorption in remote sensing, *IEEE J. Geosc. Rem. Sens.,* GE-23, 525-633.

Gao, B. C., and Goetz, A. F. H. (1990). Column Atmospheric Water Vapor and Vegetation Liquid Water Retrievals From Airborne Imaging Spectrometer Data, *J. Geophys. Res., 95*, 3549-3564.

Gao, B.-C., Heidebrecht, K. B., & Goetz, A. F. H. (1993). Derivation of scaled surface reflectances from AVIRIS data, *Remote Sensing of Environment, 44*, 165-178.

Gao, B.-C., and Kaufman, Y. J. (1995). Selection of the 1.375-μm MODIS channel for remote sensing of cirrus clouds and stratospheric aerosols from space, *J. Atm. Sci., 52*, 4231-4237.

Gao, B.-C., & Davis, C. O. (1997). Development of a line-by-line-based atmosphere removal algorithm for airborne and spaceborne imaging spectrometers, in *SPIE Proceedings, 3118*, 132-141.

Gao, B.-C., et al. (1998). Correction of thin cirrus path radiance in the 0.4 - 1.0 μm spectral region using the sensitive 1.375-μm cirrus detecting channel, *J. Geophys. Res*., 103, 32169-32176.

Gao, B.-C., Yang, P., Han, W., Li, R.-R., and Wiscombe, W. J. (2002). An algorithm using visible and 1.38-micron channels to retrieve cirrus cloud reflectances from aircraft and satellite data*, IEEE Trans. Geosci. Remote Sensing, 40*, 1659 – 1668.

Goetz, A. F. H., Vane, G., Solomon, J., & Rock, B. N. (1985). Imaging spectrometry for Earth remote sensing, *Science, 228*, 1147–1153.

Green, R. O., Eastwood, M. L., Sarture, C. M., Chrien, T. G., Aronsson, M., Chippendale, B. J., Faust, J. A., Parvi, B. E., Chovit, C. J., Solis, M., Olah, M. R., & Williams, O. (1998). Imaging spectrometry and the Airborne Visible/Infrared Imaging Spectrometer (AVIRIS), *Remote Sensing of Environment*, *65*, 227-248.

Guanter, L., Alonso, L., Moreno, J. (2005). A method for the surface reflectance retrieval from PROBA/CHRIS data over land: application to ESA SPARC campaigns, *IEEE Transactions on Geoscience and Remote Sensing*, *43*, 2908-2917.

Hansen, J. E. and Travis, L. D. (1974). Light scattering in planetary atmospheres. *Space Science Reviews*, 16, 527-610.

Holler, R., Higurashi, A., and Nakajima, T. (2004). The GLI 380-nm channel – Application for satellite remote sensing of tropospheric aerosol, *Proc. EUMETSAT Meteorological Satellite Conference.*

Kaufman, Y. J., Wald, A., Remer, L. A., Gao, B.-C., Li, R. R., & Flynn, L. (1997). The MODIS 2.1-μm channel - Correlation with visible reflectance for use in remote sensing of aerosol, *IEEE Trans. on Geoscience and Remote Sensing*, *35*, 1286-1298.

King, M. D., et al. (1998). Remote sensing of tropospheric aerosols from space: past, present, and future, *Bull. Meteor. Soc., 80*, 2229-2259.

Kokaly, R. F., Despain, D. G., Clark, R. N., & Livo, K. E. (2003). Mapping vegetation in Yellowstone National Park using spectral feature analysis of AVIRIS data. *Remote Sensing of Environment, 84*, 437−456.

Kokaly, R. F., Asner, G. P., Ollinger, S. V., Martin, M. E., and Wessman, C. A. (2009). Characterizing canopy biochemistry from imaging spectroscopy and its application to

ecosystem studies. *Remote Sensing of Environment, 113*, S78−S91.

Kruse, F. A. (1988). Use of airborne imaging spectrometer data to map minerals associated with hydrothermally altered rocks in the northern Grapevine Mountains, Nevada and California, *Remote Sensing of Environment, 24*, 31-51.

Kruse, F. A. (2004). Comparison of ATREM, ACORN, and FLAASH atmospheric corrections using low-altitude AVIRIS data of Boulder, CO, in *Summaries of 13th JPL Airborne Geoscience Workshop,* Jet Propulsion Lab, Pasadena, CA.

Mourioulis, P., Green, R. O., & Chrien, T. G. (2000). Design of pushbroom imaging spectrometers for optimum recovery of spectroscopic and spatial information, *Applied Optics*, *39*, 2210-2220.

Qu, Z., Kindel, B. C., & Goetz, A. F. H. (2003). The high accuracy atmospheric correction for hyperspectral data (HATCH) model, *IEEE Transactions on Geoscience and Remote Sensing, 41*, 1223-1231.

Richter, R. (1990). A fast atmospheric correction algorithm applied to Landsat TM images, *International Journal of Remote Sensing*, *11*, 159-166.

Richter, R. (1996). Atmospheric correction of DAIS hyperspectral image data, *Computers & Geosciences, 22*, 785-793.

Richter, R. (1998). Correction of satellite imagery over mountainous terrain, *Applied Optics, 37*, 4004-4015.

Richter, R., & Schlaepfer, D. (2002). Geo-atmospheric processing of airborne imaging spectrometry data, Part 2: atmospheric/topographic correction, *International Journal of Remote Sensing, 23(13)*, 2631-2649.

Roberts, D. A., Yamaguchi, Y., & Lyon, R. (1986). Comparison of various techniques for calibration of AIS data, in Proceedings of the 2nd Airborne Imaging Spectrometer Data Analysis Workshop (G. Vane and A. F. H. Goetz, Eds.), *JPL Publication 86-35*, 21-30, Jet Propulsion Lab, Pasadena, CA.

Rothman, L. S., Barbe, A., Benner, D. C., Brown, L. R., et al. (2003). The HITRAN molecular spectroscopic database: edition of 2000 including updates through 2001, *Journal of Quantitative Spectroscopy and Radiative Transfer, 82*, 5-44.

Rothman, L. S., et al. (2005). The HITRAN 2004 molecular spectroscopic database, *Journal of Quantitative Spectroscopy and Radiative Transfer, 96*, 139-204.

Schaepman-Strub, G., Schaepman, M. E., Painter, T. H., Dangel, S., and Martonchik, J. V. (2006). Reflectance quantities in optical remote sensing − definitions and case studies, *Remote Sensing of Environment,* 103, 27-42.

Staenz, K., Szeredi, T., & Schwarz, J. (1998). ISDAS - A System for Processing/Analyzing Hyperspectral Data; Technical Note, *Canadian Journal of Remote Sensing, 24*, 99-113.

Tanre, D., Deroo, C., Duhaut, P., Herman, M., Morcrette, J. J., Perbos, J., & Deschamps, P. Y. (1986). Simulation of the Satellite Signal in the Solar Spectrum (5S), User's Guide (U.S.T. de Lille, 59655 Villeneuve d'ascq, France: Laboratoire d'Optique Atmospherique).

Toratani, M., Fukushima, H., Murakami, H., and Tanaka A. (2007). Atmospheric correction scheme for GLI with absorptive aerosol correction, *J. Oceonography, 63*, 525 − 532.

Torres, O., et al. (1998). Derivation of aerosol properties from satellite measurements of backscattered ultraviolet radiation: Theoretical basis, *J. Geophys. Res., 103*, 17099-17110.

Ungar, S. G. (1997). Technologies for future Landsat missions, *Photogrammetric Engineering & Remote Sensing, 63*, 901-905.

Vane, G., Green, R. O., Chrien, T. G., Enmark, H. T., Hansen, E. G., & Porter, W. M. (1993). The Airborne Visible/Infrared Imaging Spectrometer, *Remote Sensing of the Environment, 44*, 127-143.

Vermote, E., et al. (1994). "Second simulation of the satellite signal in the solar spectrum (6S), 6S User's Guide Version 1," NASA-GSFC, Greenbelt, Maryland, 134 pages.